Mon. Not. R. Astron. Soc. **323**, 47–55 (2001)

PSCz superclusters: detection, shapes and cosmological implications

S. Basilakos,[1]★ M. Plionis[2] and M. Rowan-Robinson[1]

[1]*Astrophysics Group, Imperial College London, Blackett Laboratory, Prince Consort Road, London SW7 2BW*
[2]*Institute of Astronomy and Astrophysics, National Observatory of Athens, Lofos Nimfon, Thesio, 18110 Athens, Greece*

Accepted 2000 November 14. Received 2000 November 14; in original form 2000 July 13

ABSTRACT

We study the possibility of correctly identifying, from the smooth galaxy density field of the PSCz flux-limited catalogue, high-density regions (superclusters) and recovering their true shapes in the presence of a bias introduced by the coupling between the selection function and the constant radius smoothing. We quantify such systematic biases in the smoothed PSCz density field and after applying the necessary corrections we study supercluster multiplicity and morphologies using a differential geometry definition of shape. Our results strongly suggest that filamentary morphology is the dominant feature of PSCz superclusters. Finally, we compare our results with those expected in three different cosmological models and find that the Λ cold dark matter (CDM) model ($\Omega_\Lambda = 1 - \Omega_m = 0.7$) performs better than $\Omega_m = 1$ CDM models.

Key words: galaxies: general – cosmology: theory – large-scale structure of Universe – infrared: galaxies.

1 INTRODUCTION

The study of the distribution of matter on large scales, based on redshift surveys of galaxies, provides important constraints on models of cosmic structure formation. It has been established that galaxy clusters are not randomly distributed but tend to aggregate in larger systems, the so-called superclusters (cf. Bahcall 1988 and references therein). Superclusters are the largest, isolated and dynamically unrelaxed, owing to their size, objects in the large-scale distribution of matter and thus they are ideal probes of the initial conditions that gave rise to the distribution of matter on such large scales. One's hope is that they can be used for cosmological studies in order to test theories of structure formation (cf. West 1989).

Many authors have claimed that the large-scale clustering pattern of galaxies is characterized by a filamentary and sheet-like distribution (cf. Zeldovich, Einasto & Shandarin 1982; Broadhurst et al. 1990; de Lapparent, Geller & Huchra 1991). West (1989), Plionis, Valdarnini & Jing (1992) and Jaaniste et al. (1997) studied the morphological properties (shape, size and orientation) of galaxy superclusters using ACO clusters and found, based on the simple principal axes method, that the vast majority of the superclusters are flattened triaxial objects, while Plionis et al. (1992) found a predominance of prolate (filament-like) superclusters. Further support to the filamentary case was presented recently by Sathyaprakash et al. (1998a,b) who analysed the shapes of the overdense regions using observational (*IRAS* 1.2 Jy) and N-body simulation data.

★ E-mail: s.basilakos@ic.ac.uk

Studies based on the traditional indicators of clustering, such as the two-point correlation function, do not deepen our knowledge regarding the morphology and physics of structures on large scales. Therefore, many authors have been using different approaches, based on the geometrical properties of the large-scale structure, in order to investigate such features. Indeed, different methods such as minimal spanning trees, shape statistics (cf. Sahni & Coles 1995 and references therein), genus-percolation statistics (Zeldovich et al. 1982; Gott, Dickinson & Mellot 1986; Coles & Plionis 1991; Yess & Shandarin 1996; Sahni, Sathyaprakash & Shandarin 1998) and Minkowski functionals (cf. Mecke, Buchert & Wagner 1994; Kerscher et al. 1997) have been used in order to describe the global geometrical and topological properties of the matter distribution utilizing angular and redshift surveys of galaxies, and also N-body simulations.

In this paper we use the recently completed *IRAS* PSCz redshift survey in order:

(i) to investigate whether we can reliably identify superclusters and measure their shapes in flux-limited galaxy samples;
(ii) to measure the shape and size distribution of the PSCz superclusters; and
(iii) to investigate whether these distributions can be used as a cosmological probe.

The plan of this paper is as follows. In Section 2 we describe the PSCz data that we used, in Section 3 we present the supercluster identification procedure, tests of systematic biases that enter into such a procedure and the detected PSCz superclusters, while in Section 4 we present the supercluster shape determination procedure, systematic effects that affect their shapes and the

PSCz supercluster shapes. In Section 5 we compare the PSCz results with the corresponding ones of three cosmological models and finally in Section 6 we draw our conclusions.

2 THE PSCz GALAXY SAMPLE

We use in our analysis the recently completed *IRAS* flux-limited 60-μm redshift survey (PSCz) which is described in Saunders et al. (2000). It is based on the *IRAS* Point Source Catalog and contains ∼15 500 galaxies with flux $S_{\rm lim} \geq 0.6$ Jy covering the 84 per cent of the sky. The subsample we use, defined by a limiting galaxy distance of $240\,h^{-1}$ Mpc, contains ∼11 823 galaxies.

2.1 PSCz selection function

Owing to the fact that the PSCz catalogue is a flux-limited sample there is a well-known degradation of sampling as a function of distance from the observer (codified by the so-called *selection function*). Unless one corrects for this effect the derived galaxy density field will have little to do with the true one. This is usually done by weighting each galaxy by the inverse selection function, $\phi^{-1}(r)$, assuming that the unobserved galaxies are spatially correlated with the observed ones. Note that according to the above the selection function is defined as the fraction of the galaxy number density that is observed above the flux limit at some distance r. Therefore,

$$\phi(r) = \frac{1}{\langle \rho \rangle} \int_{L_{\rm min}(r)}^{L_{\rm max}} \Phi(L)\, {\rm d}L, \tag{1}$$

where $L_{\rm min}(r) = 4\pi r^2 \nu S_{\rm lim}$ is the luminosity of a source at distance r corresponding to the flux limit $S_{\rm lim}$, $\nu = 60$ μm and $\langle \rho \rangle$ is the mean galaxy number density, given by integrating the luminosity function over the whole luminosity range, with $L_{\rm min} = 10^8\,h^2\,{\rm L}_\odot$ [since lower luminosity galaxies are not represented well in the available samples; cf. Rowan-Robinson et al. (2000)], and $L_{\rm max} = 10^{13}\,h^2\,{\rm L}_\odot$. Obviously, $\phi(r)$ is a decreasing function of distance because a smaller fraction of the luminosity function falls above the flux limit at greater distances. In this work we used a luminosity function of the form assumed by Saunders et al. (1990) with $L_* = 10^{8.45}\,h^2\,{\rm L}_\odot$, $\sigma = 0.711$, $\alpha = 1.09$ and $C = 0.0308$ (cf. Rowan-Robinson et al. 2000).[1]

2.2 PSCz galaxy distances from redshifts

It is well known that the distribution of galaxies in redshift space is a distorted representation of that in real comoving space (Kaiser 1987). The redshift distance of each galaxy can by found from

$$r = \frac{2c}{H_0}[1 - (1 + z - \delta z)^{-1/2}](1 + z - \delta z)^{3/2}, \tag{2}$$

where $H_0 = 100\,h\,{\rm km\,s^{-1}\,Mpc^{-1}}$ and δz is a non-linear term to correct the redshifts for the galaxy peculiar velocities:

$$\delta z = \frac{1}{c}[\boldsymbol{u}(r) - \boldsymbol{u}(0)] \cdot \hat{\boldsymbol{r}} \tag{3}$$

with $\boldsymbol{u}(0)$ the peculiar velocity of the Local Group (LG) and $\boldsymbol{u}(r)$ the galaxy peculiar velocity at position $\boldsymbol{r}$, which can be found in linear theory by

$$\boldsymbol{u}(r) = \frac{H_0\beta}{4\pi} \int \delta(\boldsymbol{r})\, \frac{\boldsymbol{r} - \boldsymbol{r}'}{|\boldsymbol{r} - \boldsymbol{r}'|^3}\, {\rm d}^3\boldsymbol{r}, \tag{4}$$

where $\beta = \Omega^{0.6} b^{-1}$, assuming linear biasing between the background matter and the galaxy fluctuation field δ. Note that heliocentric redshifts are first transformed to the Local Group frame using $cz \simeq cz_\odot + 300\sin(l)\cos(b)$ and then the distance to each galaxy is usually found by iteratively solving the above set of equations. Such a procedure was used by Branchini et al. (1999) to recover the true density field of *IRAS* PSCz galaxies in order to study the galaxy density and velocity fields. In our work we use their results (for $\beta = 1.0, 0.5$ and 0.1) which were kindly provided to us by Dr Branchini.

2.3 Incomplete sky coverage

In order to produce a continuous and whole-sky density field it is essential to treat the 16 per cent of the sky which is devoided of data (galactic plane, high cirrus emission areas and unobserved regions). We use the PSCz data of Branchini et al. (1999), in which they followed the method of Yahil et al. (1991) to fill the galactic plane region with synthetic objects that reproduce the mean density of galaxies in the regions residing nearby. At higher galactic latitudes they fill the masked regions again with synthetic objects so that they reproduce the overall mean number density of PSCz galaxies.

3 IDENTIFYING SUPERCLUSTERS IN THE SMOOTH PSCz DENSITY FIELD

3.1 Smoothing procedure

For the purpose of this study we need to derive from the discrete distribution of PSCz galaxies a smooth continuous density field. To this end we use a Gaussian kernel on an N^3 grid:

$$\mathcal{W}(|\boldsymbol{x}_j - \boldsymbol{x}_{\rm g}|) = (2\pi R_{\rm sm}^2)^{-3/2} \exp\left(-\frac{|\boldsymbol{x}_j - \boldsymbol{x}_{\rm g}|^2}{2R_{\rm sm}^2}\right). \tag{5}$$

The smoothed density, at the grid-cell positions $\boldsymbol{x}_{\rm g}$, is then

$$\rho(\boldsymbol{x}_{\rm g}) = \frac{\sum_j \rho(\boldsymbol{x}_j)\mathcal{W}(|\boldsymbol{x}_j - \boldsymbol{x}_{\rm g}|)}{\int \mathcal{W}(|\boldsymbol{x}_j - \boldsymbol{x}_{\rm g}|)\, {\rm d}^3x}, \tag{6}$$

where the sum is over the distribution of galaxies with positions $\boldsymbol{x}_j$.

In our study we will use two smoothing radii, namely $R_{\rm sm} = 5$ and $10\,h^{-1}$ Mpc, to probe essentially different supercluster sizes. We will extend our analysis out to $r_{\rm max}$, where $r_{\rm max} = 150$ and $240\,h^{-1}$ Mpc, respectively, for the two smoothing radii, while the size of each cell is set equal to $R_{\rm sm}$. Therefore, we use a grid of size of 60^3 and 48^3, respectively. Note also that $|\boldsymbol{x}_j - \boldsymbol{x}_{\rm g}| \leq 3R_{\rm sm}$ and thus the integral in the denominator of equation (6) has a value ≃0.97.

In order to construct our supercluster candidates we select all cells with an overdensity above a chosen threshold and join together those having common boundaries. Owing to the fact that superclusters should be identified as very high-density peaks, the critical value of the overdensity threshold is defined directly from the probability density function as its 97 percentiles value (using lower values we tend to percolate structures through the whole volume).

[1] Note that we have tested the robustness of the results, presented in this paper, against the use of different selection functions (cf. Branchini et al. 1999) and found that they remain mostly unaffected.

3.2 Correcting biases introduced by smoothing

Owing to the drop of the selection function as a function of distance, shot-noise effects increase with distance. Although Gaztañaga & Yokoyama (1993) have shown that the smoothing process itself considerably suppresses such shot-noise effects, the coupling between the selection function and the constant radius smoothing will result in a distorted smoothed density distribution, especially at large distances. We expect that Gaussian spheres, centred on distant cells, will overestimate the true density in regions where galaxies are detected [owing to the large $\phi(r)$ weighting], while in underdense regions they will underestimate the true density.

The decrease of resolution, owing to the drop of the selection function at large distances, can be dealt with by increasing the smoothing radius as a function of distance. Using the mean inter-galaxy separation as the Gaussian smoothing radius is usually a good rule-of-thumb criterion to suppress such effects in cosmographical and velocity field studies. However, it cannot be used to identify and study supercluster shapes or in studies of the probability density function (PDF) and its moments, in which it is necessary to have a constant resolution element through out the studied volume.

3.2.1 Quantification of the effect

We quantify this effect by using *N*-body simulations for which we have the overall three-dimensional (3D) 'galaxy' distribution and the corresponding PSC*z* look-alike distributions (a detailed study of the effect and of the devised correction procedure on the corresponding PDF statistics will be presented in Plionis, Basilakos & Rowan-Robinson, in preparation). Here we just note that we use a CHDM ($\Omega_{\rm hot}=0.3$, $\Omega_{\rm cold}=0.6$ and $\Omega_{\rm b}=0.1$) simulation based on an optimized version of the truncated Zeldovich approximation (TZA), described in detail in Borgani et al. (1995). There are 256^3 grid points and as many particles, while the simulation box has $L=480\,h^{-1}$ Mpc and periodic boundaries. The choice of the CHDM model was based solely on the fact that the corresponding distribution of particles that we tag as 'galaxies' have a correlation length that resembles that of the *IRAS* galaxies ($r_0\simeq 4\,h^{-1}$ Mpc).

The main question that we want to answer now is: How are the 'PSC*z*'-based smoothed density field relates to the corresponding true underlying 3D density field? We answer this question by comparing the smoothed 3D distribution of the parent population of simulated '*IRAS*' galaxies with that of the corresponding PSC*z* look-alikes, generated from this distribution. We generate 10 mock 'PSC*z*' look-alike samples, centring each virtual observer in different positions of the simulation box, and we derive the statistical deviation of each smoothed 'PSC*z*' look-alike distribution from the corresponding 3D one, as a function of distance. Therefore, we evaluate the following quantity:

$$\Delta(r,\delta r)=\frac{\rho_{\cdot\rm PSCz'}(r)-\rho_{\rm 3d}(r)}{\rho_{\rm 3d}(r)}. \qquad (7)$$

in shells with width $\delta r=10\,h^{-1}$ Mpc. If the selection process does not affect the 'PSC*z*'-based density field then $\Delta(r)$, on average, should be negligible for all distances. Apparently, this seems to be the case since we do find $\Delta(r)\simeq 0$ for all distances (broken line in Figs 1 and 2). However, if we split the 'PSC*z*' densities into two subsamples: one higher and one lower than $\langle\rho\rangle$, then we find a strong distant dependent effect (see Figs 1 and 2), where the coupling between the selection function and the constant radius smoothing results in an underestimate and overestimate of the low- and high-density regions, respectively, especially at large distances.

We can attempt to fit $\Delta(r)$ using a high-degree polynomial and then correct the raw smoothed PSC*z* densities by weighting them with the factor $W(r)=[1+\Delta_{\rm fit}(r)]^{-1}$. We have, however, to note that any such multiplicative correction procedure cannot correct (artificial) zero densities. To this end we use a six-degree polynomial and a χ^2 minimization procedure to test the goodness-of-fit. The fit, presented in Figs 1 and 2 as continuous lines, has a reduced χ^2 value of <1 indicating that the fit is good, although the scatter is probably underestimated.

However, as a check of the independence of our procedure on different background cosmologies, we have also estimated the function $\Delta(r)$ utilizing a spatially flat, low-density cold dark matter model (ΛCDM), with $\Omega_0=0.2$, $h=1$, $\sigma_8=1.3$ and cosmological constant $\Omega_\Lambda=0.8$ (cf. Bahcall & Cen 1992; Dalton et al. 1994) and we found similar results. In Plionis et al. (in preparation) we will present details on the correction procedure and the results in recovering the underlying PDF and its moments. Here we test our procedure in recovering the true number, size, multiplicity function and shapes of overdense regions (see below).

3.2.2 Robustness of supercluster identification

The above-mentioned systematic effect should also affect the

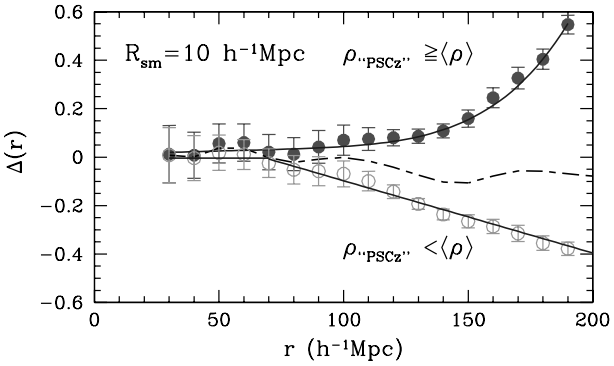

Figure 1. $\Delta(r)$ as a function of distance for the simulation smooth density field with $R_{\rm sm}=10\,h^{-1}$ Mpc. Filled symbols represent fluctuation values for $\rho_{\cdot\rm PSCz'}>\langle\rho\rangle$ while open circles represent $\rho_{\cdot\rm PSCz'}<\langle\rho\rangle$. The continuous lines represents the best polynomial fit to $\Delta(r)$ and the broken line represents $\Delta(r)$ on average.

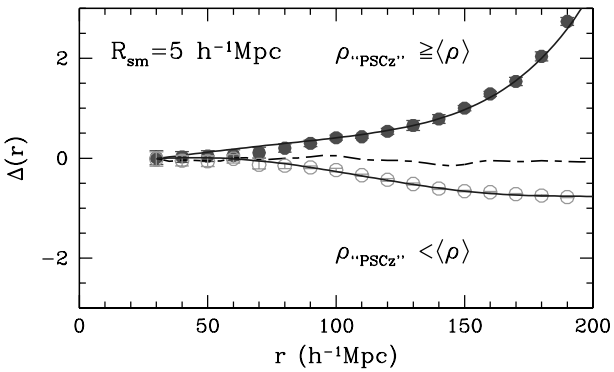

Figure 2. Same as for Fig. 1 but for the $R_{\rm sm}=5\,h^{-1}$ Mpc case.

connectedness of overdense regions and thus the detected supercluster number, size and shape. To this end we compare the number density of superclusters, found by our method in the smoothed 3D simulation distribution with the average found in 10 'PSCz' realizations. As discussed before, we select cells that have an overdensity value above a specific quantile of the PDF. However, since we are interested in comparing the superclusters found in flux-limited samples with the true underlying superclusters we have to make sure that we are using equivalent thresholds. Such a choice is easy in the simulation test case, in which we know a priori the true 3D PDF. We have found that in general a specific quantile of the raw 'PSCz' look-alike PDF is significantly larger than the corresponding 3D PDF, an effect that our density correction procedure restores to a good degree, especially in the PDF high-density tail (Plionis et al., in preparation). Therefore, we use as our density threshold a specific PDF quantile.

In Fig. 3 we compare the supercluster numbers in equal-volume shells ($\delta V \simeq 1.16\times10^7\,h^{-3}\,\mathrm{Mpc}^3$ for the $R_{\rm sm}=10\,h^{-1}$ Mpc case and $\delta V \simeq 2.83\times10^6\,h^{-3}\,\mathrm{Mpc}^3$ for the $R_{\rm sm}=5\,h^{-1}$ Mpc case) as a function of distance for the 3D, raw-'PSCz' and corrected-'PSCz' distributions. For the $R_{\rm sm}=10\,h^{-1}$ Mpc case we find that the mean supercluster number density per equal-volume shell is 17 ± 13, 10.9 ± 3 and 9.3 ± 3.3 for the 'raw', 'corrected' and true 3D density fields, while the corresponding densities for the $R_{\rm sm}=5\,h^{-1}$ Mpc case are 30 ± 13, 13 ± 4 and 14 ± 3.

It is evident that for the 'raw-PSCz' case the supercluster number density increases artificially with distance; at large distances the galaxy sampling rate is low and the smoothing procedure is unable to produce a continuous density field, producing a large number of artificially disjoint regions. This effect is efficiently suppressed once we correct the smoothed density distribution according to our correction procedure for both smoothing scales used.

In Fig. 4 we present the multiplicity function of the identified superclusters. Again we see that our correction procedure is effective in recovering the underlying multiplicity function.

We conclude that the connectedness of overdense regions in flux-limited samples, with a selection function similar to that of *IRAS* 0.6-Jy galaxies, can be recovered once we correct the 'raw' smoothed density field according to our procedure. We have verified, however, that in order to restore such connectedness we need to correct the smoothed density field limiting ourselves to within $\sim230\,h^{-1}$ Mpc for the $R_{\rm sm}\geq10\,h^{-1}$ Mpc case and to within $\sim150\,h^{-1}$ Mpc for the $R_{\rm sm}\geq5\,h^{-1}$ Mpc case.

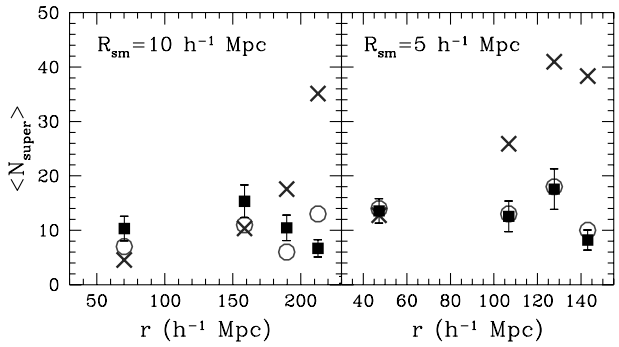

Figure 3. Supercluster numbers in equal-volume shells as a function of distance for the 3D (open circles), raw-'PSCz' (crosses) and corrected-'PSCz' (squares) cases. Errorbars represent uncertainties resulting from the 10 different 'PSCz' look-alike realizations.

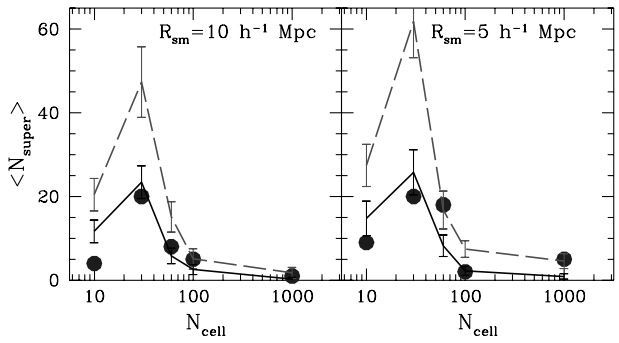

Figure 4. Supercluster multiplicity function for the 3D (points), raw-'PSCz' (broken line) and corrected-'PSCz' (continuous line) cases. Error bars are as in the previous figure.

3.3 Space density and multiplicity of PSCz superclusters

In Fig. 5 we present the space density of PSCz superclusters in equal-volume shells (for $\beta=1.0$), having the same size as that in the previous section, before and after correcting the density field according to our procedure. We have also verified that variations of δV do not alter our results.

For the $R_{\rm sm}=10\,h^{-1}$ Mpc case, in which we are revealing relatively large structures, we find in the uncorrected density field that the first shell ($\lesssim130\,h^{-1}$ Mpc), contains no supercluster, which evidently is false since it is well known that within this distance there are several superclusters such as the Great Attractor, Perseus–Pisces, Coma etc. We also observe the systematic increase of supercluster space density with distance in both $R_{\rm sm}$

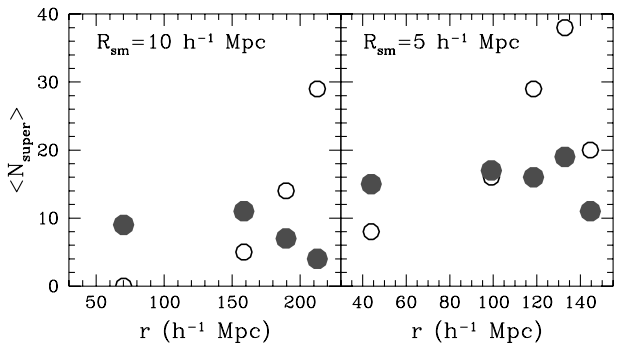

Figure 5. Mean number density of PSCz superclusters in equal-volume shells, based on the corrected (full circles) and uncorrected (open circles) smooth density fields.

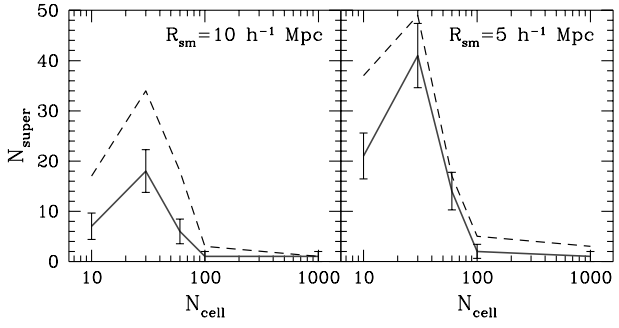

Figure 6. Multiplicity function of PSCz superclusters for the corrected (continuous line) and uncorrected (broken line) smooth density fields.

cases. However, once we correct the density field according to our procedure, discussed in Section 3.2, we recover a constant space density of superclusters in the different equal-volume shells.

In Fig. 6, we present the PSC*z* supercluster multiplicity function (for $\beta = 1.0$), for the uncorrected (broken line) and corrected density fields (continuous line), which will be used in the final section as a cosmological probe.

In Tables 1 and 2 we present for both smoothing scales, the detected PSC*z* superclusters, having a volume above the indicated threshold, and also their shape parameters (see Section 4). We have identified most of the known superclusters but also quite a few new ones. Many other known superclusters, not shown in the tables, have been found but fall below the specific volume threshold.

For the purpose of illustration we present in Figs 7 and 8 the three-dimensional map of the detected PSC*z* superclusters for the $R_{\rm sm} = 10$ and $5\,h^{-1}$ Mpc smoothed density fields, respectively, as seen from a virtual observer at a 30° inclination angle from the Supergalactic plane.

4 3D SUPERCLUSTER SHAPES

4.1 Shape determination method

The supercluster shapes are defined by fitting ellipsoids to the data. Shapes are estimated for those 'superclusters' that consist of eight or more cells. To this end we use the moments of inertia method (cf. Carter & Metcalfe 1980; Plionis, Barrow & Frenk 1991): $I_{11} = \sum w_i x_i^2$, $I_{22} = \sum w_i y_i^2$, $I_{12} = I_{21} = \sum w_i x_i y_i$, $I_{13} = I_{31} = \sum w_i x_i z_i$, $I_{23} = I_{32} = \sum w_i y_i z_i$, with w_i the statistical weight of each cell. This is defined as the density fluctuation:

$$w_i = \frac{\rho_i(x_{\rm g}) - \langle\rho\rangle}{\langle\rho\rangle}, \tag{8}$$

where $\langle\rho\rangle$ is the mean galaxy number density. Note that because of its symmetry we diagonalize the inertia tensor

$$\det(I_{ij} - \lambda^2 M_3) = 0 \qquad (M_3 \text{ is a } 3\times 3 \text{ unit matrix}), \tag{9}$$

obtaining the eigenvalues I_1, I_2, I_3, from which we define the shape of the configuration since the eigenvalues are directly related to the three principal axes of the fitted ellipsoid. The corresponding eigenvectors provide the direction of the principal axes.

4.2 Geometrical shape statistics

To identify the characteristic morphological features of superclusters and to investigate the geometrical properties of the large-scale structure, we will use the differential geometry approach, introduced by Sahni et al. (1998).

Table 1. Detected superclusters in the $R_{\rm sm} = 10\,h^{-1}$ Mpc density field with $V > 2.5\times 10^4\,h^{-3}$ Mpc^3 ($N_{\rm cell} \geq 25$) and distance $\leq 210\,h^{-1}$ Mpc.

Volume ($10^4\,h^{-3}$ Mpc^3)	$\langle d\rangle$ (h^{-1} Mpc)	$X_{\rm sup}$	$Y_{\rm sup}$	$Z_{\rm sup}$	K_1	K_2	K_1/K_2	Name
41	146	40	−140	−13	0.095	0.113	0.839	Pisces
70	177	−85	−102	−118	0.104	0.076	1.368	
36	195	10	−101	−167	0.067	0.126	0.534	
30	148	−107	−96	35	0.084	0.095	0.886	
38	201	−187	−75	−10	0.012	0.016	0.745	
27	152	104	−55	−95	0.018	0.020	0.888	
103	171	−157	58	38	0.149	0.098	1.510	Far Shapley
51	136	−117	70	−4	0.049	0.083	0.585	Near Shapley
33	110	−32	75	74	0.092	0.065	1.415	Hercules
40	159	−55	95	−115	0.043	0.066	0.645	Near Horologium

Table 2. Detected superclusters in the $R_{\rm sm} = 5\,h^{-1}$ Mpc density field with $V > 3.5\times 10^3\,h^{-3}$ Mpc^3 ($N_{\rm cell} \geq 28$) and distance $\leq 140\,h^{-1}$ Mpc.

Volume ($10^3\,h^{-3}$ Mpc^3)	$\langle d\rangle$	$X_{\rm sup}$	$Y_{\rm sup}$	$Z_{\rm sup}$	K_1	K_2	K_1/K_2	Name
4.1	134	46	−125	0	0.054	0.118	0.458	Pisces
4.1	137	−94	−96	31	0.044	0.058	0.764	
6.0	108	59	−78	48	0.057	0.033	1.697	
6.0	105	32	−58	−81	0.112	0.215	0.522	
3.5	123	52	−46	102	0.111	0.048	2.328	
4.9	89	72	−47	−24	0.054	0.082	0.655	
5.0	128	26	−36	−120	0.060	0.074	0.805	Lepus
5.4	138	95	−46	−90	0.049	0.054	0.908	
7.0	49	−39	−24	18	0.078	0.113	0.692	Pavo–Indus
7.0	49	46	−14	−9	0.116	0.053	2.205	Perseus–Pegasus
15.1	44	−36	19	−15	0.080	0.055	1.460	Great Attractor
6.3	137	−118	49	50	0.029	0.037	0.779	
11.8	132	−114	67	−1	0.071	0.158	0.445	Near Shapley
3.9	107	87	52	−32	0.000	0.000	–	
5.5	110	−43	77	65	0.055	0.138	0.400	Hercules
9.0	119	−25	75	89	0.090	0.196	0.459	
3.5	78	3	77	14	0.002	0.002	0.851	Coma/A1367
7.3	124	−14	107	61	0.063	0.106	0.591	
6.8	126	−44	108	−47	0.033	0.063	0.517	
3.6	137	4	122	−63	0.045	0.108	0.418	

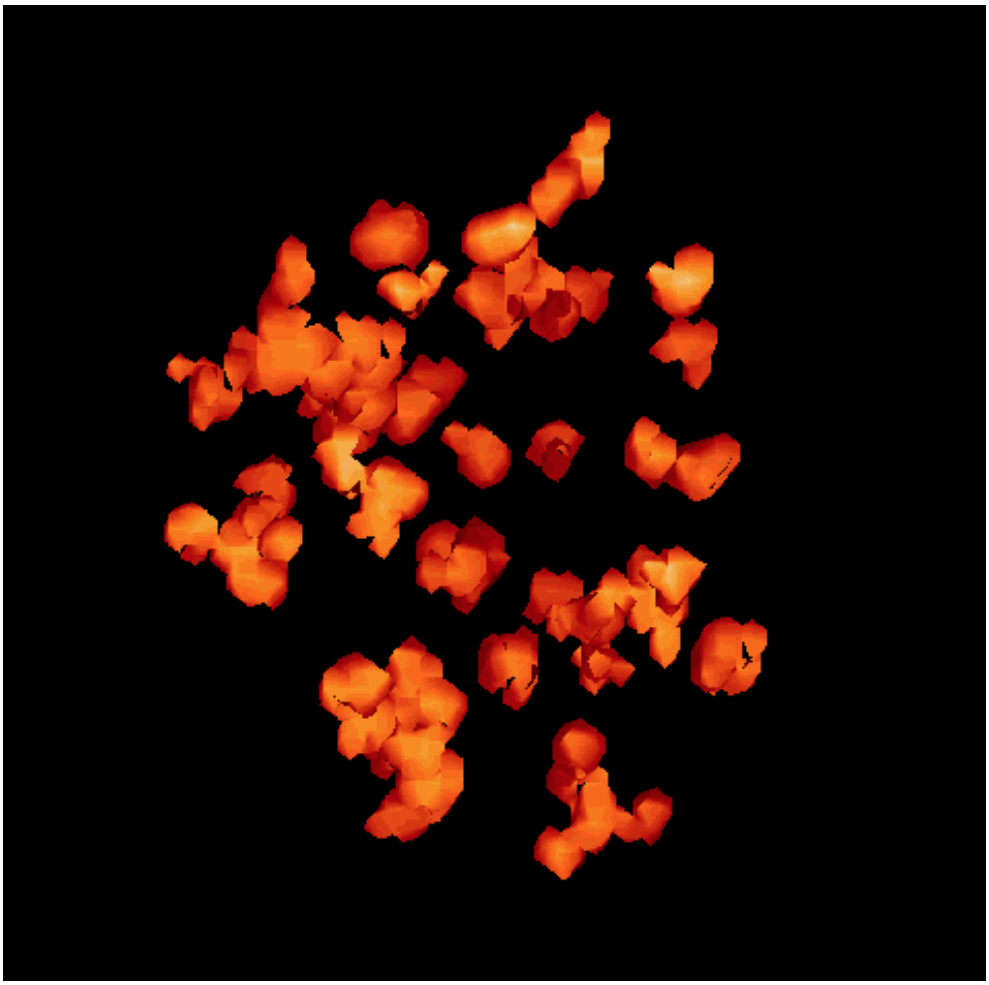

Figure 7. The map of the PSCz superclusters using $R_{\rm sm} = 10\,h^{-1}$ Mpc and within $240\,h^{-1}$ Mpc.

We remind the reader of the basic elements of differential geometry theory (cf. Lipschutz 1969). Assuming a local coordinate system on a surface with the integrating class $\mathcal{C}^2$, it is well known that the geometrical features of the surface are described by the first and second fundamental forms:

$$\boldsymbol{I} = \mathrm{d}\boldsymbol{r}\cdot\mathrm{d}\boldsymbol{r} = E\,\mathrm{d}\theta^2 + 2F\,\mathrm{d}\theta\mathrm{d}\phi + G\,\mathrm{d}\phi^2 \tag{10}$$

$$\boldsymbol{II} = -\mathrm{d}\boldsymbol{r}\cdot\mathrm{d}\boldsymbol{n} = L\,\mathrm{d}\theta^2 + 2M\,\mathrm{d}\theta\mathrm{d}\phi + N\,\mathrm{d}\phi^2, \tag{11}$$

where[2] $E = \boldsymbol{r}_\theta\cdot\boldsymbol{r}_\theta$, $G = \boldsymbol{r}_\phi\cdot\boldsymbol{r}_\phi$, $F = \boldsymbol{r}_\theta\cdot\boldsymbol{r}_\phi$, $L = \boldsymbol{r}_{\theta\theta}\cdot\boldsymbol{n}$, $G = \boldsymbol{r}_{\phi\phi}\cdot\boldsymbol{n}$ and $M = \boldsymbol{r}_{\theta\phi}\cdot\boldsymbol{n}$ ($\boldsymbol{n}$ is the perpendicular vector $\boldsymbol{n} = \boldsymbol{r}_\theta\times\boldsymbol{r}_\phi/|\boldsymbol{r}_\theta\times\boldsymbol{r}_\phi|$). Thus, the surface area, integrated mean curvature and genus can be written as

$$S = \int\int\sqrt{EG - F^2}\,\mathrm{d}\theta\mathrm{d}\phi \tag{12}$$

$$C = \int\int\tfrac{1}{2}(k_1 + k_2)\,\mathrm{d}S \tag{13}$$

$$\mathcal{G} = \frac{-1}{4\pi}\int\int k_1k_2\,\mathrm{d}S, \tag{14}$$

where

$$k_1 + k_2 = \frac{EN + GL - 2FM}{EG - F^2} \tag{15}$$

[2] $\boldsymbol{r}_\alpha = \frac{\partial\boldsymbol{r}}{\partial\alpha}$ and $\boldsymbol{r}_{\alpha\alpha} = \frac{\partial^2\boldsymbol{r}}{\partial\alpha^2}$.

and

$$k_1k_2 = \frac{LN - M^2}{EG - F^2}. \tag{16}$$

The genus parameter characterizes the surface topology; multiply connected surfaces have $\mathcal{G} > 0$, while simply connected ones have $\mathcal{G} < 0$.

Furthermore, we define the three-dimensional shape of structures by fitting the best triaxial ellipsoid ($M = 0$),

$$\boldsymbol{r}(\theta,\phi) = I_1\sin\theta\cos\phi\,\hat{\boldsymbol{i}} + I_2\sin\theta\sin\phi\,\hat{\boldsymbol{j}} + I_3\cos\theta\,\hat{\boldsymbol{k}},$$

to the different isodensity contours having volume $V = \frac{4}{3}\pi I_1I_2I_3$ and $0 \le \phi \le 2\pi$, $0 \le \theta \le \pi$.

Here we present the basic steps of the shape statistics that we will use, following the notation of Sahni et al. (1998). They introduced a set of three shapefinders $\mathcal{H}_1 = VS^{-1}$, $\mathcal{H}_2 = SC^{-1}$ and $\mathcal{H}_3 = C$, having dimensions of length. In the same framework they defined two-dimensional shapefinders $K = (K_1, K_2)$, where

$$K_1 = \frac{\mathcal{H}_2 - \mathcal{H}_1}{\mathcal{H}_2 + \mathcal{H}_1} \tag{17}$$

and

$$K_2 = \frac{\mathcal{H}_3 - \mathcal{H}_2}{\mathcal{H}_3 + \mathcal{H}_2}, \tag{18}$$

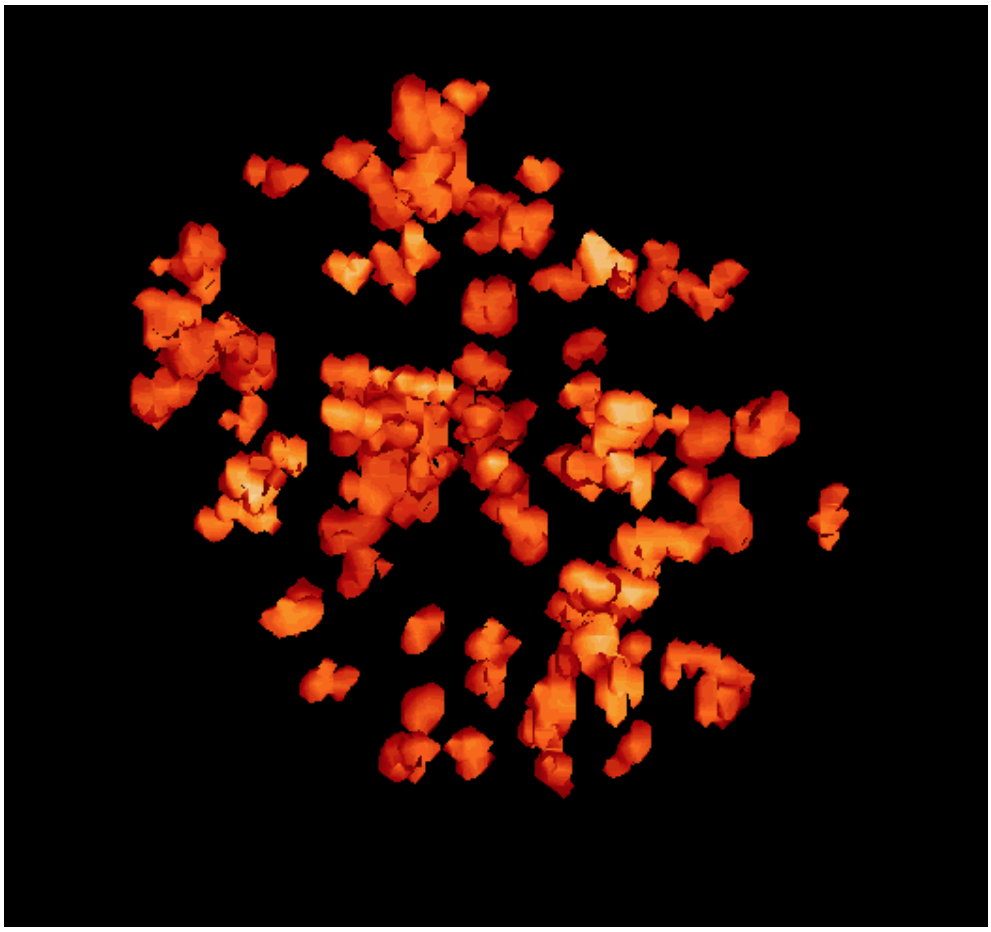

Figure 8. The map of the PSCz superclusters using $R_{\rm sm} = 5\,h^{-1}$ Mpc and within $150\,h^{-1}$ Mpc.

normalized to give $\mathcal{H}_i = R$ ($K_{1,2} = 0$) for a sphere of radius R. Therefore, based on these shapefinders we can characterize the morphology of cosmic structures according to the following categories:

(i) pancakes for $K_1/K_2 > 1$;
(ii) filaments for $K_1/K_2 < 1$;
(iii) ribbons for $(K_1, K_2) = (\alpha, \alpha)$ with $\alpha \leq 1$ and thus $K_1/K_2 \simeq 1$;
(iv) sphere for $I_1 \simeq I_2 \simeq I_3$ and thus $(K_1, K_2) \simeq (0, 0)$;
(v) ideal filament (one-dimensional objects) for $\mathcal{H}_1 \simeq \mathcal{H}_2 \ll \mathcal{H}_3$ and thus $(K_1, K_2) \simeq (0, 1)$;
(vi) ideal pancake (two-dimensional object) for $\mathcal{H}_1 \ll \mathcal{H}_2 \simeq \mathcal{H}_3$ and thus $(K_1, K_2) \simeq (1, 0)$.

Finally, for the quasi-spherical objects the $K_{1,2}$ are small and therefore their ratio (K_1/K_2) measures the deviation from spherical shapes.

4.3 Robustness of supercluster shape determination

Here we investigate how the systematic effects, discussed in Section 3.2, affect the determination of supercluster shapes. To this end we compare the shapes of the superclusters, found by our method in the smoothed 3D simulation distribution with those found in 10 'PSCz' realizations.

Performing many tests using different smoothing radii, we have found that the ratio of the dimensionless supercluster shapefinders

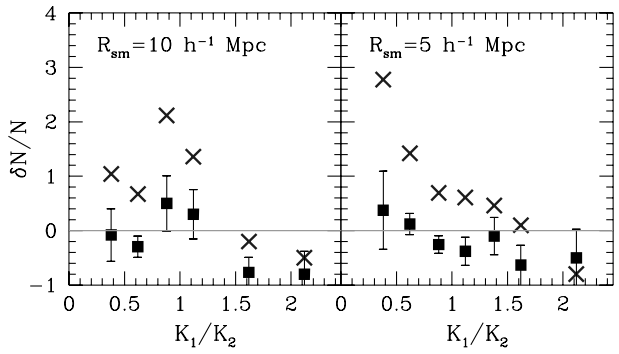

Figure 9. Shape spectrum fluctuations between the 3D and raw-'PSCz' case (crosses) and between the 3D and the corrected-'PSCz' case (squares). Error bars represent uncertainties resulting from the 10 different 'PSCz' look-alike realizations.

('shape spectrum') is also affected from the bias discussed above. Note that we exclude the ideal spherical surfaces, $I_1 \simeq I_2 \simeq I_3$, because their ratio K_1/K_2 tends to infinity. In Fig. 9 we present the fluctuations of the shape spectrum between the 3D and raw-'PSCz' case and between the 3D and the corrected-'PSCz' case. Again it is evident that our correction procedure suppresses significantly the systematic effects introduced by the coupling between the selection function and the constant-radius smoothing for both smoothing radii.

We conclude that in order to correctly identify superclusters and

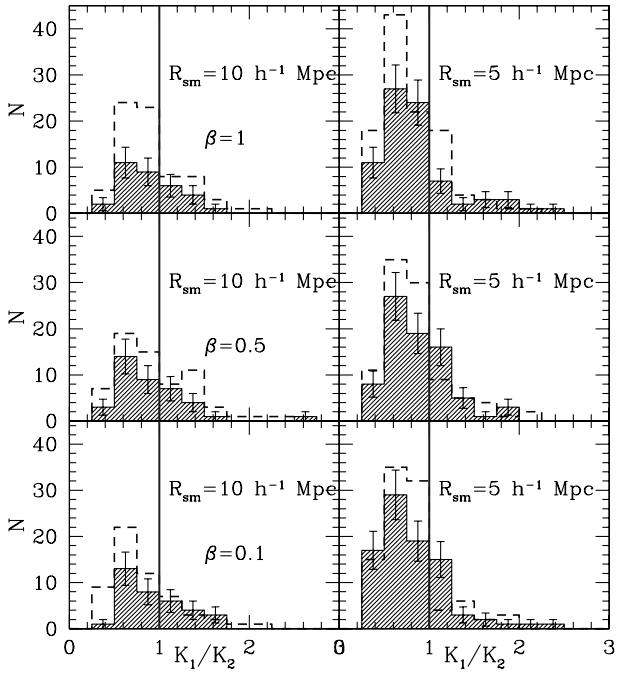

Figure 10. The corrected (hatched region) and uncorrected (broken line) shape spectrum of PSCz superclusters for the three reconstructions of the PSCz density field (see Branchini et al. 1999) and for two smoothing radii.

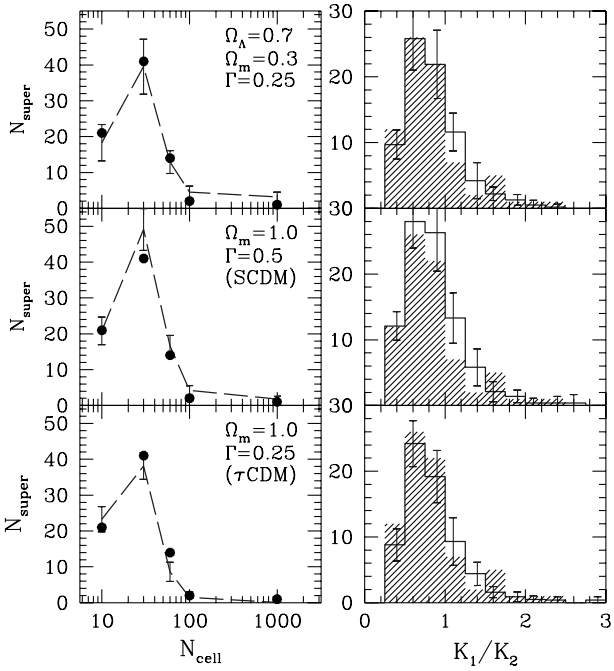

Figure 11. PSCz Superclusters comparison with Cosmological models: Left-hand panel, multiplicity function; right-hand panel, shape spectrum. The PSCz results are represented by filled symbols and hatched regions.

their connectedness, and their shapes from flux-limited samples, it is necessary to take into account the bias of the smoothed density field, discussed in Section 3.2, and correct accordingly the smoothed galaxy distribution.

4.4 The PSCz supercluster shape spectrum

In Fig. 10 we present the uncorrected and corrected 'shape spectrum' for three reconstructions of the PSCz density field, namely for $\beta = 1.0$, 0.5 and 0.1, and for both smoothing radii. It is obvious that the dominant feature of the PSCz superclusters (for all β) is the filamentary type structure, i.e. $K_1/K_2 < 1$ [in agreement with previous studies; see Sathyaprakash et al. (1998a,b)]. We see only a weak tendency to have less filamentary superclusters for reconstructions with $\beta < 1$.

Furthermore, although the fraction of filamentary superclusters ($K_1/K_2 < 1$) remain roughly the same before and after the correction, there is a slight change of the corrected 'shape spectrum' towards less extreme filamentary superclusters.

Regarding extreme shaped superclusters (with $N_{\rm cell} \geq 8$), we have found, in the $R_{\rm sm} = 5\,h^{-1}$ Mpc smoothed field, eight very filamentary superclusters with $K_1/K_2 < 0.45$ (among which the Near Shapley and Hercules superclusters), six spherical and only two extreme pancake-like structures with $K_1/K_2 > 2$ (one of which is the Perseus–Pegasus supercluster; see Table 2). In the $R_{\rm sm} = 10\,h^{-1}$ Mpc smoothed field we find only one such extreme filamentary supercluster.

5 COMPARISON WITH COSMOLOGICAL MODELS

We use mock PSCz catalogues, generated from three large cosmological N-body simulations, in order to investigate whether supercluster properties (shapes and numbers) can discriminate between models. The cosmological simulations are based on an AP^{3}M code and they are described in Cole et al. (1998). We consider three different cold dark matter models:

(i) a flat low-density CDM model with $\Omega_{\rm m} = 1 - \Omega_\Lambda = 0.3$;

(ii) a critical density universe $\Omega_{\rm m} = 1$ with power spectrum $\Gamma = 0.25$ (τCDM); and

(iii) a critical density universe $\Omega_{\rm m} = 1$ with power spectrum $\Gamma = 0.5$ (SCDM).

The first two models are normalized by the observed cluster abundance at zero redshift; having fluctuation amplitude in $8\,h^{-1}$ Mpc scale of $\sigma_8 = 0.55\Omega_{\rm m}^{-0.6}$ (Eke, Cole & Frenk 1996), while the third is *COBE* normalized with $\sigma_8 = 1.35$.

For each cosmological model we average results over 10 nearly independent mock PSCz catalogues extending out to a radius of $170\,h^{-1}$ Mpc (cf. Branchini et al. 1999). Good care has been taken to centre the catalogues to suitable LG-like observers (having similar to the observed Local Group velocity, shear and overdensity).

We analyse the mock PSCz catalogues density fields (with $R_{\rm sm} = 5\,h^{-1}$ Mpc) in the same fashion as that of the observed PSCz catalogue and we compare the outcome of this procedure in Fig. 11, where we plot the detected supercluster shape spectrum and multiplicity function for all three models and PSCz data. Evidently, the SCDM model performs worst in the comparison. In order to quantify the differences between models and data we perform a standard χ^2 test, assuming Gaussianly distributed errors, and we present the $\mathcal{P}_{>\chi^2}$ results in Table 3. The only model that is excluded by the data at a relatively high significance level is the SCDM model, while the ΛCDM model best reproduces the observed supercluster shape spectrum and multiplicity function. The τCDM is marginally excluded by the multiplicity function comparison but only at a ~ 94 per cent level.

Table 3. χ^2 probabilities ($\mathcal{P}_{>\chi^2}$) of consistency between data and models, and between the models themselves.

Comparison pair	Shape spectrum	Multiplicity function.
PSCz–ΛCDM	0.148	0.135
PSCz–SCDM	0.019	0.019
PSCz–τCDM	0.146	0.06
ΛCDM–SCDM	0.71	5.2×10^{-3}
ΛCDM–τCDM	0.94	6.6×10^{-4}
τCDM–SCDM	0.07	2×10^{-8}

Comparing the models among themselves we see that the shape spectrum is insensitive to the different cosmologies, probably because supercluster shapes reflect the Gaussian nature of the initial conditions which are common to all models. However, the supercluster multiplicity function is a strong discriminant between the models and therefore our results do show a preference of the ΛCDM model over the $\Omega_{\rm m} = 1$ models that we have studied.

6 CONCLUSIONS

We have studied the properties of superclusters detected in the smoothed PSCz galaxy density field as connected regions above some overdensity threshold. We have investigated, using simulations, the biases that enter into the detection and shape determination of superclusters which are identified in smoothed density fields of flux-limited galaxy samples.

We have devised a statistical approach to correct for such biases and we have verified that it indeed recovers the underlying 3D properties of superclusters. To determine supercluster shapes we use the differential geometry approach of Sahni et al. (1998) and find that the dominant supercluster morphology is filamentary.

Finally, we have compared our PSCz supercluster results with the corresponding ones generated from the analysis of three cosmological models (SCDM, τ-CDM and ΛCDM) and we find that the model that best reproduces the observational results is the ΛCDM model ($\Omega_\Lambda = 0.7$).

ACKNOWLEDGMENTS

We thank Enzo Branchini for providing us with his reconstructed PSCz galaxy distribution and the PSCz mock catalogues and S. Cole for generating the simulations from which the mock catalogues have been extracted. We also thank S. Borgani for providing us with the Zeldovich approximation simulations. Andreas Efstathiou and Seb Oliver are greatfully acknowledged for their help in using IDL to produce the 3D PSCz supercluster maps. MP acknowledges the hospitality of the Astrophysics Group of Imperial College, where a major part of this work was done. This work was supported by EC Network programme 'POE' (grant number HPRN-CT-2000-00138).

REFERENCES

Bahcall N. A., 1988, Ann. Rev. Astron. Ap., 26, 631
Bahcall N. A., Cen R., 1992, ApJ, 398, L11
Borgani S., Plionis M., Coles P., Moscardini L., 1995, MNRAS, 277, 1210
Branchini E., Plionis M., 1996, ApJ, 460, 569
Branchini E. et al., 1999, MNRAS, 308, 1
Broadhurst T. J., Ellis R. S., Koo D. C., Szalay A. S., 1990, Nat, 343, 726
Carter D., Metcalfe J., 1980, MNRAS, 191, 325
Coles P., Plionis M., 1991, MNRAS, 250, 75
Cole S., Hatton S., Weinberg D. H., Frenk C. S., 1998, MNRAS, 300, 945
Davis M., Efstathiou G., Frenk C. S., White S. D. M., 1985, ApJ, 292, 371
de Lapparent V., Geller M. J., Huchra J. P., 1991, ApJ, 369, 273
Eke V., Cole S., Frenk C. S., 1996, MNRAS, 282, 263
Gaztanaga E., Yokoyama J., 1994, ApJ, 403, 405
Gott J. R., Dickinson M., Melott A. L., 1986, ApJ, 306, 341
Jaaniste J., Einasto M., Einasto J., Andernach H., Muller V., 1997, A&A, 329, 1
Kaiser N., 1987, ApJ, 284, L9
Kerscher M. et al., 1997, MNRAS, 284, 73
Lipschutz M. M., 1969, Theory and Problems of Differential Geometry. McGraw-Hill, New York
Mecke K. R., Buchert T., Wagner H., 1994, A&A, 288, 697
Nolthenius R., Klypin A., Primack J. R., 1994, ApJ, 422, 45
Plionis M., Barrow J. D., Frenk C. S., 1991, MNRAS, 249, 662
Plionis M., Valdarnini R., Jing Y. P., 1992, ApJ, 398, 12
Rowan-Robinson M. et al., 2000, MNRAS, 314, 37
Sahni V., Coles P., 1995, Phys. Rep., 262, 1
Sahni V., Sathyaprokash B. S., Shandarin S., 1998, ApJ, 495, L5
Sathyaprakash S. B., Sahni V., Shandarin S., 1998a, ApJ, 508, 551
Sathyaprakash S. B., Sahni V., Shandarin S., Fisher B. K., 1998b, ApJ, 507, L109
Saunders W., Rowan-Robinson M., Lawrence A., Efstathiou G., Kaizer N., Ellis R. S., Frenk C. S., 1990, MNRAS, 242, 318
Saunders W. et al., 2000, MNRAS, 317, 55
Stompor R., Górski K. M., Banday A. J., 1995, MNRAS, 277, 122
West J. M., 1989, ApJ, 347, 610
Yahil A., Strauss M., Davis M., Huchra J. P., 1991, ApJ, 372, 380
Yess C., Shandarin S., 1996, ApJ, 465, 2
Zeldovich Ya. B., A&A, 4, 84
Zeldovich Ya. B., Einasto J., Sandarin S., 1982, Nat, 300, 407

This paper has been typeset from a TEX/LATEX file prepared by the author.